

Cite this: *RSC Appl. Interfaces*, 2024,  
1, 977

# Mechanistic insight into the role of the aspect ratio of nanofillers in the gas barrier properties of polymer nanocomposite thin films†

Subhash Mandal,<sup>a</sup> Debmalya Roy,<sup>a,b</sup> Kingsuk Mukhopadhyay,<sup>b</sup>  
Mayank Dwivedi<sup>c</sup> and Mangala Joshi<sup>a</sup>

The introduction and processing parameters of 2D graphene flakes into a polymer matrix were altered in order to understand the impact of dispersed flake geometry on the physical properties of nanocomposites. It has been highlighted in this study that the intermolecular interaction plays a critical role in the structure-properties of polymeric barrier films where the experimental results were validated by appropriate models. The microstructural analysis of nanocomposite films revealed that 2D nanofillers predominantly existed in an agglomerated state inside the polymer matrix and the size of the nanofiller cluster linearly increased as a function of loading percentage. We have illustrated that the immobilization of nanotubes into graphene flakes creates a porous hierarchical geometry which facilitates the polymer chains to diffuse into hybrid nanofillers to produce a uniform phase segregated morphology. Our findings underscore the significance of the aspect ratio of dispersoids in influencing the barrier properties of nanocomposite flexible films.

Received 30th October 2023,  
Accepted 26th April 2024

DOI: 10.1039/d3lf00214d

rsc.li/RSCApplInter

## 1. Introduction

Polyurethane (PU) stands out as a unique class of block copolymers, boasting a blend of flexible and rigid segments. These polymers exhibit a wide range of desirable characteristics, including exceptional elasticity, excellent low-temperature flexibility, strong tensile strength, good abrasion resistance, chemical resistance, and ease of processing.<sup>1–3</sup> In addition to their adaptable characteristics, PUs find application across a diverse spectrum, including coatings, adhesives, sealants, flexible and rigid foams, paints, varnishes, leathers, rubbers, fibers, films, biomimetic materials, and many other domains.<sup>1,4,5</sup>

Nevertheless, PUs bear a substantial drawback: they exhibit inherent permeability to various gases and vapors, encompassing oxygen (O<sub>2</sub>), nitrogen (N<sub>2</sub>), carbon dioxide (CO<sub>2</sub>), helium (He), water, and organic vapors. When compared to alternative polymeric barrier materials, PUs fall short in terms of gas barrier properties, as indicated in Table 1. It is worth noting, however, that the permeability of

different gases through PU films and membranes varies considerably, contingent upon the structure and morphology of the PU material.<sup>6–10</sup>

Recent trends have witnessed the extensive use of certain polymers, such as biaxially oriented polyester (BoPET, Mylar®), ethylene vinyl alcohol copolymer (EVOH), and polyvinylidene chloride (PVDC, Saran®), in gas barrier applications. Nevertheless, most of these polymers lack attributes like low-temperature flexibility, weatherability, resistance to flex fatigue, and adhesion. Moreover, many of them are not heat-sealable.<sup>4</sup> In contrast, polyurethane excels in all these aspects, albeit its gas barrier properties are a challenge.

The stringent requirement for effective gas barrier properties is particularly critical in specialized applications where PU-based membranes, films, or coatings are extensively employed. These applications encompass coated or laminated envelopes used in lighter-than-air (LTA) applications like hot air balloons, aerostats, and airships, as well as food packaging, automotive uses including primer coatings and tires, biomedical applications such as dialysis membranes, wound dressings, encapsulating membranes, and catheters, as well as flame retardant and anticorrosion coatings.<sup>1,11,12</sup> However, the notable permeation of gases through PU-based films and coatings severely compromises their performance in these scenarios.

The nature of PU as a block copolymer, composed of hard and soft segments, inherently leads to phase separation due

<sup>a</sup> Indian Institute of Technology Delhi, Hauz Khas, New Delhi-110016, India.  
E-mail: mangala@textile.iitd.ac.in

<sup>b</sup> Nanoscience & Coating Division, DMSRDE, DRDO, G T Road, Kanpur-208013, India. E-mail: droy.dmsrde@gov.in

<sup>c</sup> DMSRDE, DRDO, G T Road, Kanpur-208013, India

† Electronic supplementary information (ESI) available. See DOI: <https://doi.org/10.1039/d3lf00214d>

**Table 1** Gas permeability of various polymeric and elastomeric films under standard testing conditions<sup>1,4,6–10</sup>

Polymer/elastomer	Permeability (cm <sup>3</sup> mm m <sup>-2</sup> per day per atm)				Ref.
	Carbon dioxide (CO <sub>2</sub> )	Oxygen (O <sub>2</sub> )	Nitrogen (N <sub>2</sub> )	Helium (He)	
Ethylene vinyl alcohol copolymer (EVOH)	0.03–0.08	0.01–0.05	0.003–0.01	4–14	1, 4
Polyvinylidene chloride (PVDC)	0.47–3.2	0.03–0.04	0.02–0.12	—	1, 9, 10
Liquid crystal polymer (Vectran)	—	0.05–0.1	0.03–0.5	—	1, 9, 10
Nylon 6	1.8–5.9	0.57–1.3	0.28–0.35	45.7	1, 9, 10
Polyvinylidene fluoride (PVDF)	2.2–30	0.55–5.2	3–3.5	59–86	1, 9, 10
Nylon 6,6	3–4.6	0.3–1.36	0.28	59.1	1, 9, 10
Polyvinyl fluoride (PVF)	4.4	1.3	0.1	59.1	1, 4
Biaxially oriented polyester (BoPET)	5.9–9.8	1–2.4	0.18–0.39	71	1, 9, 10
Vinylidene fluoride-hexafluoropropylene copolymer	209–508	71–95	4.67–22	771	1, 9, 10
Low-density polyethylene (LDPE)	394–959	69–274	394–959	—	1, 4
Polytetrafluoroethylene (PTFE)	487–720	178–255	69–129	—	1, 9, 10
Fluorinated ethylene-propylene copolymer (FEP)	648–838	101–290	33–125	—	1, 4
Polyurethane (PU)	175–2014	3–1067	9–297	36–2340	1, 4, 6, 7, 8
Silicon rubber	118 110	19 685	17 280	—	1, 4

to thermodynamic disparities between these segments. This phase separation represents the primary reason for the elevated gas permeability observed in PU films and coatings. While some efforts have been made to enhance PU's gas barrier properties through chemical modifications, morphology alterations, and the careful selection of components, composition, and preparation conditions, these approaches have yielded only moderate improvements.<sup>13–17</sup>

A promising avenue for significantly improving PU's gas barrier properties involves the incorporation of impermeable lamellar or nanoplatelet-like fillers, such as clay or graphene, distinguished by their high aspect ratios.<sup>18–20</sup> The inclusion of these nanoplatelets disrupts the diffusion path of gaseous molecules, compelling the permeant molecules to follow longer and more convoluted routes during diffusion through PUNC films, ultimately resulting in enhanced gas barrier properties.<sup>7,8,21</sup> Remarkably, even small loadings of these inorganic phases, when well-dispersed, can lead to a significant enhancement in the gas barrier properties of the host matrix, sometimes up to 500 times. These fillers, known as passive fillers, greatly amplify the tortuosity encountered by gas molecules during their journey through the polymer. The effectiveness of a passive inorganic filler is contingent upon its volume fraction, aspect ratio, distribution, and orientation.

In addition to passive fillers, there are also reactive fillers, such as functionalized graphene, carbon nanotubes (CNTs), polyhedral oligomeric silsesquioxane (POSS), and nanocellulose, capable of forming reactions or crosslinks with the host matrix. This leads to an improvement in the gas barrier properties of polymers like PU.<sup>22,23</sup> Researchers also reported soft liquid metal-infused conductive sponges that directly indicate the flexibility of polyurethane even after reinforcement with inorganic fillers.<sup>24</sup> The critical requirement for LTA applications is a high barrier against helium gas. Thus, the study's objective is to improve the helium gas barrier properties of polyurethane films.

Graphene, a single-atom-thick, sp<sup>2</sup> hybridized, 2D planar sheet of carbon arranged in a honeycomb crystal lattice,

possesses remarkable properties.<sup>25,26</sup> Owing to its plate-like structure and tiny geometric pore size (0.064 nm), graphene has significant potential for enhancing the gas barrier properties of polymers by increasing the tortuosity of the gas diffusion path.<sup>27,28</sup> Despite its ultrathin nature (1.153 nm), graphene sheets are impermeable to gases, including helium.<sup>1,29–31</sup> Therefore, this study highlights the improvement of the gas barrier properties of aliphatic PU films by incorporating and dispersing edge-functionalized few-layer graphene.

The interaction between the filler and polymer, along with the method of preparing polymer nanocomposites, plays a crucial role in controlling the dispersion of nanofillers in the polymer matrix and, consequently, the properties of nanocomposites. In this study, hybrid 3D nanofillers (CNTs were immobilized into the few-layer graphene to enhance the dispersion and distribution of few-layer graphene by maintaining a higher aspect ratio) were employed to enhance the interaction between PU and functionalized few-layer graphene. Furthermore, a novel process route was followed to achieve excellent dispersion of hybrid 3D nanofillers in the nanocomposites. This approach involved a supramolecular self-assembly route followed by twin screw extrusion. Films were then produced from these nanocomposites and their helium gas barrier properties were thoroughly examined. The films were also evaluated by attenuated total reflection Fourier transform IR (ATR-FTIR), scanning electron microscopy (SEM), transmission electron microscopy (TEM), wide angle X-ray diffraction (WAXD), and atomic force microscopy (AFM) techniques. The 2 wt% hybrid 3D nanofiller-reinforced polyurethane nanocomposite film exhibited excellent gas barrier performance, reducing helium gas permeability by a substantial 63%. The widely accepted models for predicting gas permeability of polymer nanocomposites *viz.* the Nielsen model, Bhardwaj model and Cussler-random array have been used to correlate and validate the experimentally found results.



## 2. Theory of gas permeability: mechanism, measurement and modelling

The details on the theory of gas permeability mechanism, measurement and modelling are provided in section S1 of the ESI† in which (i) the gas transport mechanism in polymer films and polymer nanocomposite membranes and (ii) the process of measuring gas permeability across polymeric membranes or films are discussed in sections S1.1 and S1.2† respectively.

### 2.1. Theoretical frameworks for forecasting the gas barrier characteristics of polymer nanocomposite materials

The enhancement in barrier characteristics of polymer nanocomposites is ascribed to the dispersion of nanoplatelets, such as clay and graphene, within the polymer matrix. This arrangement creates a convoluted route that obstructs the movement of gas molecules, thereby impeding their permeation.<sup>32</sup> Numerous scientists have put forth diverse models aimed at elucidating the gas transmission behaviour across polymer nanocomposites that incorporate inorganic nanoplatelets.<sup>33–36</sup> In accordance with the solution–diffusion model,<sup>32</sup> the permeability ( $P$ ) of gases and vapors across polymer membranes results from the multiplication of the gas or vapor's solubility ( $S$ ) within the polymer matrix and its diffusivity ( $D$ ) through the same matrix, as illustrated in equation:  $P = D \times S$ . The relationship between the volume fraction of the filler and the solubility of gas molecules in the polymer nanocomposites is as follows:

$$S = S_0(1 - \varphi) \quad (1)$$

Here, the symbol  $\varphi$  represents the volume fraction of fillers, and  $S_0$  denotes the solubility attributed to the pure polymer matrix.<sup>37</sup> The diffusivity within the nanocomposite is contingent upon the tortuosity of diffusion pathways within the membrane, and their correlation is expressed as:

$$D = D_0/\tau \quad (2)$$

In this context,  $\tau$  represents tortuosity, and  $D_0$  signifies the diffusivity pertaining to the unperturbed polymer matrix.<sup>38</sup> Tortuosity ( $\tau$ ) is defined as the quotient of the distance covered by a gas traversing the polymer nanocomposite membrane or film ( $l'$ ) and the thickness of the said membrane or film ( $l$ ). This relationship can be formulated as expressed in ref. 31:

$$\tau = l'/l \quad (3)$$

The magnitude of  $\tau$  relies upon both the volume fraction and the geometry of the nanofillers. Numerous investigators have computed  $\tau$  for various filler varieties. Specifically, in the presence of nanoplatelets within the polymer matrix, there is

an augmentation in the gas diffusion distance. This increment can be determined using the subsequent relationship:

$$l' = l + N\frac{L}{2} = l + \frac{lL\varphi}{2w} \quad (4)$$

where ' $w$ ' and ' $L$ ' denotes the width and length of the nanoplatelets, respectively, that are dispersed in a polymer matrix, and  $N$  denotes the quantity of nanoplatelets and is expressed by:  $N = l\varphi/w$ . After substituting eqn (4) into eqn (3), we obtain the expression for equation of tortuosity:<sup>39</sup>

$$\tau = 1 + \left(\frac{L}{2w}\right)\varphi = 1 + \frac{\alpha}{2}\varphi \quad (5)$$

where  $\alpha$  represents the aspect ratio ( $L/w$ ) of the nanoplatelets.

**2.1.1. Influence of nanoplatelets' volume fraction and aspect ratio.** Numerous scholars have formulated empirical frameworks for estimating gas permeability across polymer nanocomposites, considering the impact of tortuosity and the structural characteristics of these nanocomposites. In 1967, Nielsen introduced an initial model to assess the relative permeability of polymer–clay nanocomposites compared to pristine polymers.<sup>33</sup> Nielsen postulated an orderly configuration of two-dimensional rectangular nanoplatelets, assuming complete exfoliation and precise alignment perpendicular to the direction of diffusion. The depicted representation of this model is as follows:

$$\frac{P}{P_0} = \frac{1 - \varphi}{\tau} \quad (6)$$

$P$  represents the gas permeability across polymer nanocomposites,  $P_0$  signifies the gas permeability of the pristine polymer matrix, and  $P/P_0$  stands for the polymer nanocomposites' relative permeability ( $R_p$ ). Upon substituting the expression from eqn (5), the equation can be reformulated as follows:

$$\frac{P}{P_0} = \frac{1 - \varphi}{1 + \left(\frac{\alpha}{2}\right)\varphi} \quad (7)$$

This equation elucidates that the relative permeability diminishes as the aspect ratio and volume fraction of nanoplatelets increase. The anticipated variations in relative gas permeability for diverse aspect ratios and volume fraction values ( $\varphi$ ) are graphically depicted in Fig. 1.

In practical application, eqn (7) holds true exclusively for  $\varphi$  values up to 0.1, as higher values of  $\varphi$  often result in nanoplatelet aggregation.<sup>31</sup> Subsequently, Cussler *et al.*<sup>35</sup> introduced a modification to Nielsen's model, postulating a scenario where well-aligned nanoplatelets are dispersed randomly within a polymer matrix. The formulation of Cussler's model is presented below:

$$\frac{P}{P_0} = \frac{1}{1 + \mu\alpha^2\left(\frac{\varphi^2}{1 - \varphi}\right)} = \frac{1 - \varphi}{1 - \varphi + \mu\alpha^2\varphi^2} \quad (8)$$

In this equation,  $\mu$  represents a geometric factor intrinsic to the random porous medium, influenced by the geometrical



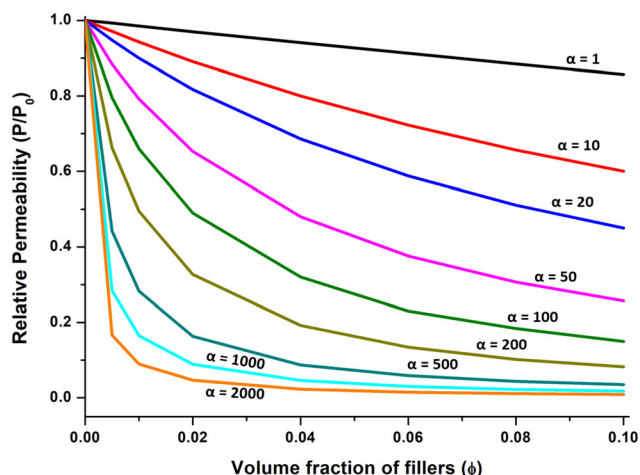


Fig. 1 Predictions from Nielsen's model regarding the relative permeability of polymer nanocomposites concerning the volume fraction of platelets, considering various particle aspect ratios.

attributes of plate-like particles, including their shape, size irregularities, and the degree of positional disorder.<sup>36</sup> The distinguishing feature between these two models lies in the fact that Nielsen's model assumes an extremely low concentration of fillers, featuring an ordered alignment of platelets. On the other hand, Cussler's model, often called a semi-dilute system, applies to scenarios with a higher filler concentration, where randomly sized, strongly aligned, and spaced flakes are prevalent, making it more suitable for membranes.

Numerous models rely on the concept of an idealized flake-filled membrane. This membrane encompasses flakes possessing a width denoted as '2d' and a thickness denoted as 'a'. These flakes are separated by a distance marked as 'b' and extend infinitely within the plane of the page. The gap or separation between the flakes is represented by 's'.

A few more models in this context are discussed in S1.3.1 in the ESI.† Other factors *viz.* (i) the influence of nanoplatelet orientation, (ii) the influence of the interfacial regions, (iii) the influence of the state of delamination and the dispersion characteristics of nanoplatelets within the polymer matrix and (iv) the influence of the number of layers in nanoplatelets and the phenomenon of their aggregation that affect the gas barrier properties are discussed in sections S1.3.2, S1.3.3, S1.3.4 and S1.3.5, respectively, in the ESI.†

## 3. Experimental

### 3.1. Materials

For this study, we obtained a commercial aliphatic polyether-based TPU known as Texin SUN-3006, which is an extrusion-grade material with a hardness rating of 90 Shore A, a specific gravity of 1.08 g cm<sup>-3</sup>, and molecular weight characteristics of approximately Mn = 79 000, Mw = 211 000, and an MFI (melt flow index) of 5.1 g per 10 min at 200 °C with a load of 2.16 kg. This TPU was sourced from Covestro,

India. In our laboratory, we synthesized a hybrid 3D carbonaceous nanofiller by immobilizing multi-walled carbon nanotubes (MWCNT-COOH) onto edge-functionalized few layer graphene (FLG-OH).<sup>40,41</sup> The schematic representation of this hybrid 3D carbonaceous nanofiller is illustrated in Fig. 2.

### 3.2. The process of preparing nanocomposites and their subsequent film formation

The hybrid 3D carbonaceous nanofiller was introduced into the TPU matrix through two distinct processing methods: (i) Twin screw extrusion (TSE) and (ii) supramolecular self-assembly route (SSAR), followed by TSE. The concentration of the nanofillers was varied as 0.25, 0.5, 1.0, 2.0 and 5.0 wt% (0.15, 0.3, 0.6, 1.2, and 3.0 vol%). To prepare films of neat TPU and TPU nanocomposites, we employed a hot pressing technique. Neat TPU pellets and granules or chips of PU nanocomposites were used for this purpose. The process took place in a compression molding machine (Carver Inc.). The TPU pellets were carefully positioned between two finely finished Teflon-coated fabric layers, and this assembly was placed inside a film mold made from the same fabric material. Subsequently, the assembly was hot-pressed under a pressure of 1.36 MPa for a specific duration and then allowed to cool, resulting in films with a consistent thickness of approximately 150 μm. The composition details of compression molded films of hybrid 3D nanofiller reinforced polyurethane nanocomposites prepared through SSAR followed by TSE and direct TSE are given in Table 2.

### 3.3. Characterization and testing

The analysis and characterization of the materials were conducted using various techniques as follows: ATR-FTIR spectra were recorded using a high-resolution ATR-FTIR instrument from Perkin Elmer (Spectrum 100 series). The spectra were collected in the range of 4000–600 cm<sup>-1</sup> with a resolution of 4 cm<sup>-1</sup>, and an average of 8 scans was taken for each sample. A zinc selenide (ZnSe) crystal was used as the ATR element. Morphological studies were performed using a SUPRA 40 VP Gemini scanning electron microscope from Carl Zeiss. The accelerating voltage used was 10 kV. Prior to

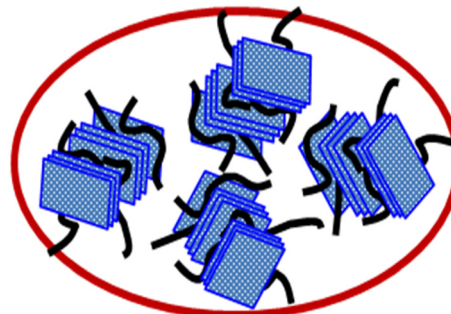


Fig. 2 Schematic of the hybrid 3D carbonaceous nanofiller.





**Table 2** Composition details of polyurethane nanocomposite films

TPU/3D by SSAR-TSE		TPU/3D by direct TSE	
Sample code	Conc. of filler (wt%)	Sample code	Conc. of filler (wt%)
TPU	0	TPU	0
TPU/3D/SSAR-TSE/0.25	0.25	TPU/3D/TSE/0.25	0.25
TPU/3D/SSAR-TSE/0.5	0.5	TPU/3D/TSE/0.5	0.5
TPU/3D/SSAR-TSE/1.0	1.0	TPU/3D/TSE/1.0	1.0
TPU/3D/SSAR-TSE/2.0	2.0	TPU/3D/TSE/2.0	2.0
TPU/3D/SSAR-TSE/5.0	5.0	TPU/3D/TSE/5.0	5.0

imaging, the samples were coated with a thin layer of vacuum-deposited gold. Wide angle X-ray diffraction (WAXD) patterns of both neat PU and the cellular structure of PU nanocomposites were recorded using a Bruker AXS diffractometer from Germany (D8 Advance). The X-rays were generated in a sealed tube, with a wavelength of 0.154 nm (Cu K-alpha). TEM samples were prepared through ultra cryomicrotomy using a Leica Ultracut UCT. Sharpened glass knives with a cutting edge of 45° were used to obtain cryosections with a thickness of approximately 50–60 nm at a temperature of –80 °C. These cryosections were collected on copper grids (mesh size 300) and examined using a TEM (JEM-2010, JEOL, Japan) operated at an accelerating voltage of 200 kV. The hybrid 3D nanofiller, pure polyurethane (PU), and PU nanocomposite films were examined using a confocal laser dispersion Raman microscope from Renishaw in the United Kingdom. The Raman spectra were acquired across a wavelength range spanning 400 to 3200 cm<sup>–1</sup>, with a 785 nm laser serving as the excitation source. During the dynamic mechanical analysis (DMA) experiment, temperature scans were conducted using a TA Instruments model Q800 in tension mode. The experiment employed an oscillatory frequency of 1 Hz and a heating rate of 5 °C per minute. The samples used for testing had dimensions of 30 × 10 × 2 mm<sup>3</sup>. The helium gas permeability of the films was assessed using a N500 gas permeation analyzer from GBPI Packaging Instruments Co. Ltd., following the ASTM D-1434-82 standard. The tests were conducted at an average temperature of 25 °C. The helium gas transmission rate (GTR) was determined using the differential pressure method. During the measurement, the film was securely positioned in a test chamber, and a vacuum was created on both sides of the film. Helium gas was introduced into the top chamber at a constant pressure of 100 kPa. The increase in pressure and the GTR were monitored and recorded using software connected to the gas permeability testing setup. Topographic atomic force microscopy (AFM) images were acquired using an A100 SPM instrument manufactured by A.P.E. Research in Italy. To prepare the samples for imaging, solid cellular specimens were carefully sectioned and affixed onto a freshly cleaved highly oriented pyrolytic graphite substrate using double-sided carbon tape.

## 4. Results and discussion

### 4.1. Helium gas barrier properties

The barrier layer requires two important properties *viz.* mechanical and gas barrier properties. The mechanical properties have been studied for hierarchical (1D, 2D and hybrid 3D) nanofillers in TPU and reported.<sup>40,42</sup> It was found that the hybrid 3D nanofiller in TPU exhibits optimum mechanical properties. Hence, hybrid 3D nanofiller incorporated TPU nanocomposite films have been considered due to their gas barrier properties in this article. Fig. 3 illustrates the results of helium gas permeability in PU nanocomposite films as a function of hybrid 3D nanofiller concentration. Notably, as the concentration of the hybrid 3D nanofiller increased in the PU matrix, the helium gas permeability gradually decreased. Intriguingly, a significant reduction of approximately 20–24% in helium gas permeability was observed with just 0.5 wt% (0.3 vol%) of hybrid 3D nanofiller loading. This reduction was attributed to the highly effective dispersion of graphene platelets in the hybrid 3D nanofiller within the polyurethane matrix at lower loading levels. However, as the concentration of the hybrid 3D nanofiller increased further, the reduction in permeability occurred at a slower rate. This reduction in gas permeability, which led to the improved gas barrier properties of the PU nanocomposite films, was primarily due to the elongation of the tortuous path that gas molecules had to traverse through the well-dispersed and partially exfoliated nanocomposite morphology.<sup>1,43</sup> Furthermore, the presence of graphene in the matrix hindered the chain movement of PU due to hydrogen bonding, as confirmed by FTIR analysis, contributing to the enhancement of helium gas barrier properties.<sup>1,8</sup>

The lowest helium gas permeability was achieved with a 2 wt% (1.2 vol%) loading of hybrid 3D nanofillers, resulting in a remarkable 63% reduction in helium gas permeability values. A concise summary of Table 3 presents diverse values indicating the reduction in gas or permeant permeability for various nanocomposite films based on TPU and graphene or graphene oxides. Additionally, the helium gas permeability of TPU-based nanocomposite films and coatings is included.

Relative helium gas permeability values of various PU nanocomposite films were also compared with different model-predicted gas permeability values. Effective mixing and proper dispersion of nanoplatelets such as graphene or nano-clay are known to significantly enhance the gas barrier properties of polymers. The relative gas permeability ( $R_p$ ) of polymer nanocomposites can be determined using equations derived from the 'tortuous path theory'.<sup>33,50</sup> Various models are used to predict gas permeability in polymer nanocomposites, with  $R_p$  depending on factors related to the nanofiller, such as volume fraction, aspect ratio, shape, and orientation in the polymer matrix.<sup>51</sup> Among these models, the Nielsen model, Cussler-random array model, and Bharadwaj model are three simple models that calculate the  $R_p$  value of polymer nanocomposites, considering a 2D



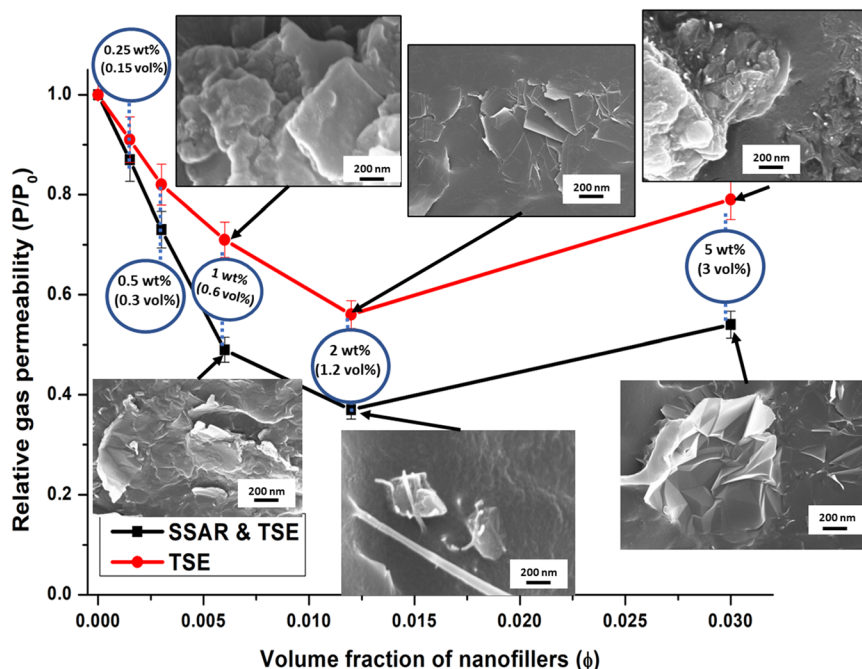


**Fig. 3** The relative helium gas permeability of films prepared using TPU nanocomposites. These nanocomposites were obtained either by incorporating hybrid 3D nanofillers using a twin-screw extruder (red line) or through a supramolecular self-assembly route followed by twin-screw extrusion (black line). SEM images of TPU nanocomposite films containing 1.0, 2.0, and 5.0 wt% of hybrid 3D nanofiller are also provided for both processing techniques.

rectangular ribbon-type filler geometry,<sup>33,34,50</sup> as summarized in Table 4.

Fig. 4 presents a comparative plot of experimental results and predictions from different models for relative helium gas permeabilities at various concentrations of 2D platelet-like nanofillers. It was observed that the actual gas permeability

did not precisely follow any specific model at higher loading levels. However, the experimental results showed a good correlation with the Cussler-random array model up to 2 wt% (1.2 vol%) loading.

Interestingly, the experimental results for relative gas permeability of PU nanocomposite films prepared using

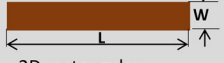
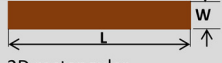
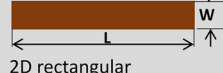
**Table 3** A brief overview of different gas/permeant permeability reduction values of various TPU/graphene or graphene oxide-based nanocomposite films and helium gas permeability of the TPU based nanocomposite films/coatings

Types of PU	Processing technique	Filler loading	Filler type	Permeability reduction (%)	Type of gas/permeant	Ref.
Polyester based TPU	Solvent mixing	1.6 vol%	iGO	94–99	N <sub>2</sub>	19, 44
Polyester based TPU	Solvent mixing	1.6 vol%	TRG	81	N <sub>2</sub>	19, 44
Polyester based TPU	Melt intercalation	1.6 vol%	TRG	52	N <sub>2</sub>	19, 44
Polyester polyol and MDI based TPU	<i>In situ</i> polymerization	1.5 vol%	TRG	71	N <sub>2</sub>	19, 44
Polyester polyol and MDI based TPU	<i>In situ</i> polymerization	1.5 vol%	HD-GNRs	62	N <sub>2</sub>	19, 44
Aliphatic, polyether based TPU	Solution mixing	0.5 wt%		99.9	N <sub>2</sub>	21
IFR-PU	Melt mixing	2 wt%	rGO	90.4	O <sub>2</sub>	45
Waterborne aliphatic PU	<i>In situ</i> polymerization	3 wt%	rGO	~76	Water vapor	46
Aliphatic polyether grade TPU	Melt mixing master batch	3 wt%	Func. graphene	30	He	47
Aliphatic polyether grade TPU	Melt mixing	3 wt%	Cloisite 30B	31	He	48
Aliphatic polyether grade TPU	Melt mixing master batch	3 wt%	Cloisite 30B	39	He	48
Aliphatic polyether grade TPU	Coating on polyester fabric	3 wt%	Cloisite 30B	58.5	He	49
3rd generation hyperbranched PU	Solution mixing	8 wt%	Cloisite 30B	76	He	18
Aliphatic polyether grade TPU	TSE	2 wt%	Hybrid 3D	44 ± 2.5	He	Experimental
Aliphatic polyether grade TPU	SSAR-TSE	2 wt%	Hybrid 3D	63 ± 2.5	He	Experimental

Note: graphene oxide is represented as GO, thermally reduced graphene oxide as TRG, reduced graphene oxide as rGO, intumescent flame-retardant polyurethane as IFR-PU, isocyanate treated graphene oxide as iGO, hexadecyl-functionalized low-defect graphene nanoribbons as HD-GNRs, and hydroxyl-modified functionalized graphene as f-G-OH. TSE is twin screw extrusion and SSAR-TSE is supramolecular self-assembly route followed by twin screw extrusion.



Table 4 A concise overview of the models<sup>33,34,50</sup>

Model name	Nielsen model	Bharadwaj model	Cussler-random array
Formula	$R_p = \frac{1 - \phi}{1 + \frac{\alpha\phi}{2}}$	$R_p = \frac{1 - \phi}{1 + \frac{\alpha}{3} \left( S + \frac{1}{2} \right) \alpha}$ $S = 1$ (planar arrangement), $S = 0$ (random arrangement) & $S = -\frac{1}{2}$ (orthogonal arrangement) of nanoplatelets	$R_p = \frac{1 - \phi}{\left( 1 + \frac{\alpha\phi}{3} \right)^2}$
Filler type	Ribbon	Ribbon	Ribbon
Orientation of nanoplatelets	Regular planar arrangement	Planar or random or orthogonal orientation	Random arrangement
Filler geometry	 2D rectangular	 2D rectangular	 2D rectangular

$R_p$ : relative permeability;  $\phi$ : nanoplatelets' volume fraction;  $S$ : order or orientation parameter;  $L$ : length of nanoplatelets;  $W$ : thickness of nanoplatelets;  $\alpha = L/W$ : aspect ratio.

nanomaterials obtained through supramolecular self-assembly followed by twin-screw extrusion correlated well with the Cussler-random array model when the aspect ratio of the FLG nanofillers ( $\alpha$ ) was 180. Conversely, for films prepared using nanomaterials obtained solely by twin-screw extrusion, the correlation was good with the Cussler-random array model at an aspect ratio of 90.

This observed behavior could be attributed to the fact that the actual dispersion state of graphene in the PU matrix may not match the ideal dispersions assumed in different models, and this state of dispersion may vary with nanofiller loading.<sup>1</sup> Thus, at specific concentrations (up to 2.0 wt%) of hybrid 3D nanofiller, the nanoplatelets might be partially exfoliated and uniformly dispersed, leading to a significant reduction in gas permeability that aligns with the predictions of the Cussler-

random array model for nanofiller aspect ratios of 180 and 90.

However, as the hybrid 3D nanofiller concentration increased, the actual gas permeability values deviated from the predictions of any particular model, likely due to changes in the dispersion state of the hybrid 3D nanofiller in the PU matrix and slight agglomeration tendencies at higher loadings (5 wt%), as observed in SEM images (Fig. 3).

#### 4.2. FTIR analysis

FTIR analysis was employed to investigate the interaction between the PU matrix and the hybrid 3D nanofiller. The ATR-FTIR spectra of neat thermoplastic polyurethane (TPU, navy blue color); polyurethane nanocomposite films reinforced with 0.25 wt% (TPU/3D/TSE/0.25, black color), 0.5 wt% (TPU/3D/TSE/0.5, red color), 1.0 wt% (TPU/3D/TSE/1.0, blue color), 2 wt% (TPU/3D/TSE/2.0, magenta color) and 5 wt% (TPU/3D/TSE/5.0, green color) hybrid 3D nanofillers by TSE in the range 4000–600  $\text{cm}^{-1}$  are shown in Fig. S3 of the ESI.† In the FTIR spectra (refer to Fig. 5a) of the hybrid 3D nanofiller, several distinctive peaks were observed, possibly attributable to the presence of oxygen-containing groups. These groups include: OH (a broad peak around 3320  $\text{cm}^{-1}$ ), C=O (at 1720, 1670 and 1388  $\text{cm}^{-1}$ ), C–O–C (at 1628  $\text{cm}^{-1}$ ), C–OH (at 1238  $\text{cm}^{-1}$ ), and C–O (at 1022  $\text{cm}^{-1}$ ).<sup>8,52,53</sup> These oxygen-containing groups have the potential to facilitate the formation of hydrogen bonds with various functional groups present in the host polyurethane matrix.<sup>54</sup>

Additionally, the peaks at 2922 and 2851  $\text{cm}^{-1}$  were assigned to asymmetric and symmetric C–H stretching, respectively, of methylene groups. Due to the presence of amide and carbonyl groups in the polyurethane, internal hydrogen bonds are formed. Notably, a faint peak at 3445  $\text{cm}^{-1}$  and a broad peak at 3319  $\text{cm}^{-1}$  were attributed to free and hydrogen-bonded N–H stretching, respectively.<sup>43,48,51</sup> The

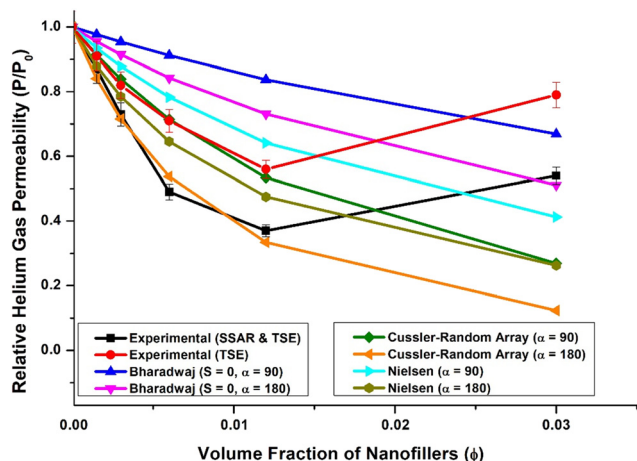


Fig. 4 The relative helium gas permeability of polyurethane (PU) nanocomposite films, strengthened with varying concentrations of hybrid 3D nanofiller, is assessed and contrasted with predicted gas permeability values from different models.



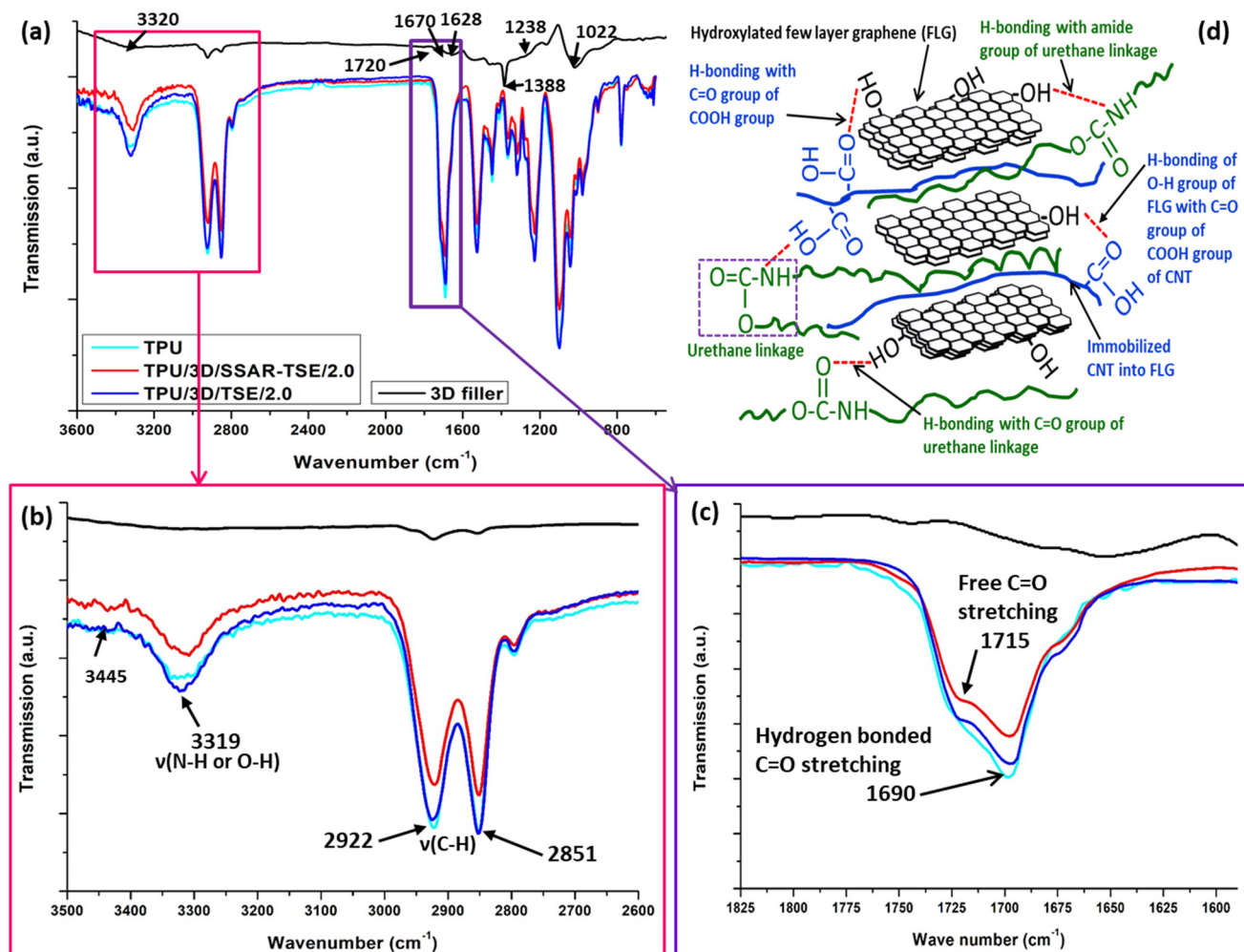


Fig. 5 FTIR spectra of the hybrid 3D nanofiller, neat PU and PU nanocomposites in the range (a) 3600–600  $\text{cm}^{-1}$ , (b) 3500–2600  $\text{cm}^{-1}$ , and (c) 1825–1590  $\text{cm}^{-1}$ , and (d) schematic of different hydrogen bonding in the hybrid 3D nanofiller incorporated PU nanocomposite.

intensity of these peaks (Fig. 5b) indicates that a majority of the N-H groups in the PU were engaged in hydrogen bonding.

Conversely, peaks at 1715  $\text{cm}^{-1}$  and 1690  $\text{cm}^{-1}$  (Fig. 5c) were associated with the stretching of free and hydrogen-bonded carbonyl groups ( $\text{C}=\text{O}$ ).<sup>43,48,55,56</sup>

The ATR-FTIR spectra of neat thermoplastic polyurethane (TPU, navy blue color); polyurethane nanocomposite films reinforced with 0.25 wt% (TPU/3D/SSAR-TSE/0.25, black color), 0.5 wt% (TPU/3D/SSAR-TSE/0.5, red color), 1.0 wt% (TPU/3D/SSAR-TSE/1.0, blue color), 2 wt% (TPU/3D/SSAR-TSE/2.0, magenta color) and 5 wt% (TPU/3D/SSAR-TSE/5.0, green color) hybrid 3D nanofillers through SSAR followed by TSE in the range 4000–600  $\text{cm}^{-1}$  are shown in Fig. S4.† In the nanocomposite TPU/3D/SSAR-TSE/2.0, the peak at 1715  $\text{cm}^{-1}$  nearly disappeared, suggesting that most of the carbonyl groups participated in hydrogen bond formation with the hybrid 3D nanofiller. In contrast, in TPU/3D/TSE/2.0, the peak was only partially reduced, indicating that some carbonyl groups remained uninvolved in hydrogen bond formation with the hybrid 3D

nanofiller. Fig. 5d shows the hydrogen bonding interactions within polyurethane (PU) nanocomposites that incorporate hybrid 3D nanofillers. These hydrogen bonds represent attractive forces involving hydrogen atoms and electronegative atoms (commonly oxygen or nitrogen) within the nanocomposite. The illustration in Fig. 5d highlights the locations and characteristics of these hydrogen bonds, offering insights into how they contribute to the nanocomposite's overall structure and properties. The strong hydrogen bonding between the functional groups of the hybrid 3D nanofiller and urethane group of TPU helps to exfoliate the FLGs in the nanocomposites. The exfoliation of FLGs decides the aspect ratio of the FLGs within the nanocomposites. The exfoliation in the process of SSAR-TSE also increased the aspect ratio of FLGs higher than direct TSE. This depiction will help to understand the hydrogen bonding network within hybrid 3D nanofiller-incorporated PU nanocomposites, which plays a crucial role in determining their performance and behaviour resulting in the reduction in helium gas barrier permeability.





### 4.3. SEM of cryo-fractured surfaces of PU nanocomposite films

SEM analysis was employed to examine the morphology and distribution of hybrid 3D nanofillers within the PU matrix. The SEM images of polyurethane nanocomposite films reinforced with hybrid 3D nanofillers of (a) 0.25 wt% and (b) 0.5 wt% by TSE; (c) 0.25 wt% and (d) 0.5 wt% through SSAR followed by the TSE technique are shown in Fig. S5.† In Fig. 3, the SEM image illustrates graphene flakes. In the process of preparing nanocomposites, the hybrid 3D nanofillers were initially dispersed into a solvent through ultrasonication. Subsequently, this dispersion was further improved through SSAR and TSE methods, resulting in a well-dispersed configuration within the PU matrix, as evident from the cryo-fractured surface of PU nanocomposite films (Fig. 3). Only when using higher loading (5 wt%) did we observe slight agglomeration of nanofillers (Fig. 3). The uniform dispersion of graphene sheets within the PU matrix can be attributed to the strong hydrogen bonding, as determined by FTIR analysis, and an effective mixing achieved through the combination of SSAR and TSE processes due to which significant reduction in helium gas permeability was found.

### 4.4. TEM analysis

Fig. 6 illustrates the dispersion state of graphene sheets within a hybrid 3D nanofiller in a PU matrix, as observed through TEM analysis for TPU/3D/TSE/2.0 and TPU/3D/SSAR-TSE/2.0 samples. After subjecting the stacks of graphene platelets within the hybrid 3D nanofillers to ultrasonication, they were successfully separated into individual platelets or thinner stacks. In the case of TPU/3D/TSE/2.0 (Fig. 6a), these graphene platelets exhibited dispersion, intercalation, and partial exfoliation. However, TPU/3D/SSAR-TSE/2.0 (Fig. 6b) displayed a more uniform dispersion and superior exfoliation, indicating effective mixing between the graphene within the hybrid 3D nanofiller and the PU matrix.

### 4.5. WAXD analysis

In Fig. 7a, the WAXD patterns of the hybrid 3D nanofiller, pure PU, and PU nanocomposite films are presented. The

broad peak in the  $2\theta$  range of  $15\text{--}25^\circ$  is characteristic of PU.<sup>43</sup> The intensity of this peak exhibited slight variations in different nanocomposites. The XRD spectra of pristine thermoplastic polyurethane (TPU, red color), and PU films incorporating 2 wt% hybrid 3D nanofillers through TSE (blue color), and SSAR followed by TSE (magenta color) clearly depict a reconstruction of the TPU microstructures. The  $2\theta$  peaks at  $20.0^\circ$  and  $22.5^\circ$  can be attributed to the amorphous halo, signifying the presence of soft domains, short-range regularly ordered hard segments, and the crystallization of hard segments, respectively.<sup>57,58</sup> The inclusion of hybrid 3D nanofillers significantly impacted the crystalline microstructure of the hard segments. The decrease in intensity of the shoulder at  $22.5^\circ$  due to the addition of nanofillers indicated that these functional nanofillers effectively penetrated the microstructural phases, leading to a reduction in the hard segments. This widening of the amorphous halo in the 3D nanofiller-reinforced microstructure suggests that the kinetics of both hard and soft segments within the TPU matrix became notably disordered due to the interpenetrating network formed by the 3D nanofiller in the TPU matrix. A reduction in the intensity of hard segments has been previously reported in waterborne PU nanocomposites incorporating functionalized graphene sheets.<sup>59</sup> The presence of nanofillers, such as CNTs and graphene flakes, or CNTs embedded within graphene flakes, is indicated by the  $2\theta$  peaks at  $26.5^\circ$ .

Graphene is distinguishable by the peak at  $2\theta = 26.5^\circ$ , originating from the (002 plane) reflection.<sup>60,61</sup> In the nanocomposites, this peak's position remained consistent. However, as the concentration of graphene in the PU matrix decreased, the peak's height diminished. Additionally, certain other peaks, such as the one at  $2\theta = 23.8^\circ$  in the X-ray diffractogram of the 3D nanofiller, were absent in the nanocomposites due to the notably lower percentage of hybrid 3D nanofiller present in the PU matrix.

### 4.6. Atomic force microscopy (AFM)

AFM investigations (Fig. 7b–d) revealed that the 3D nanofillers induced the formation of spherulites

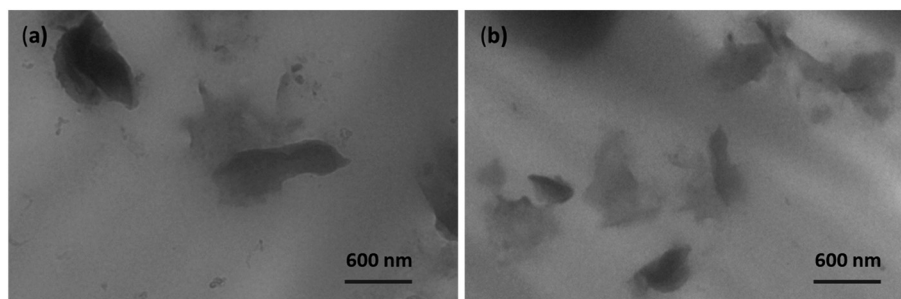


**Fig. 6** TEM images of polyurethane nanocomposite films reinforced with 2 wt% hybrid 3D nanofillers (a) by TSE and (b) through SSAR followed by the TSE technique.



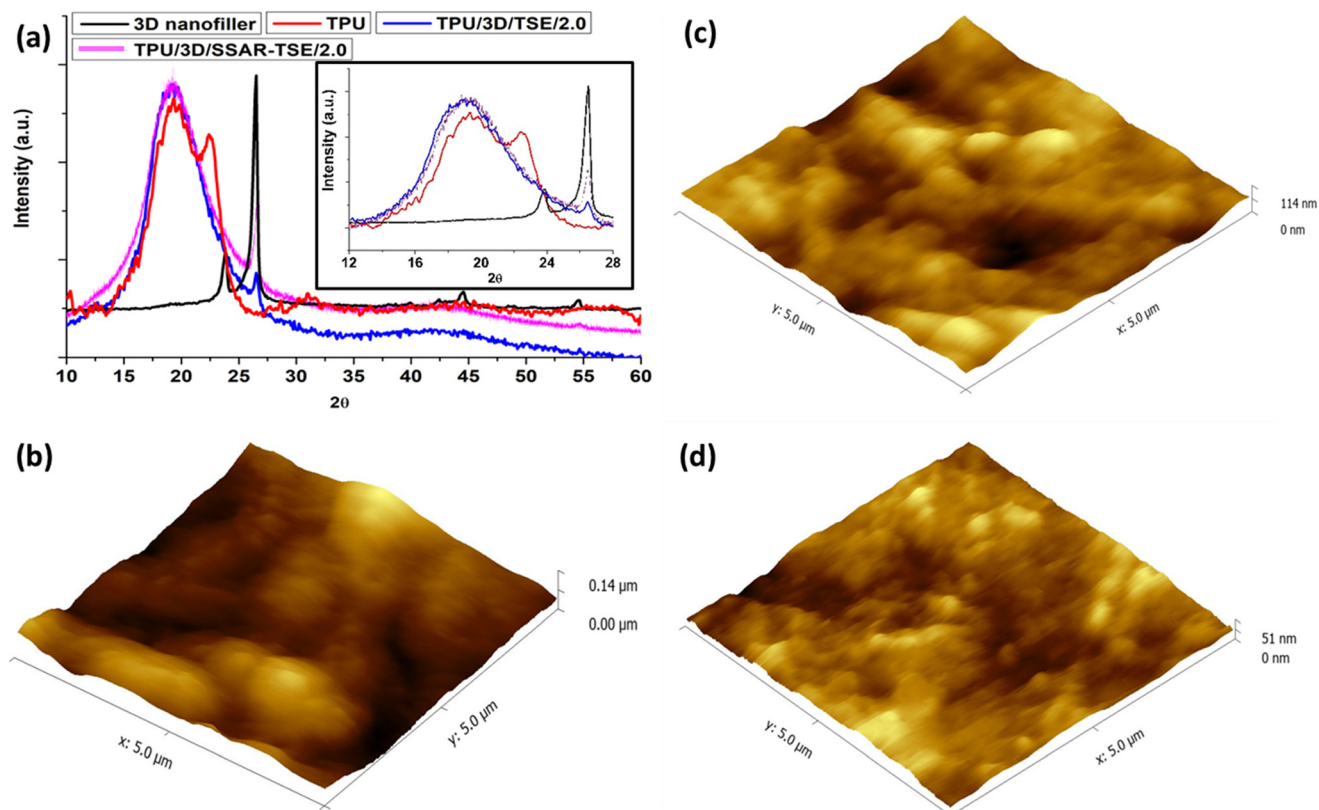


**Fig. 7** (a) WAXD of hybrid 3D nanofillers (black color), neat polyurethane (red color), 2 wt% hybrid 3D nanofiller incorporated PU film by TSE (blue color) and through SSAR followed by TSE (magenta color); AFM images (b) neat polyurethane, 2 wt% hybrid 3D nanofiller incorporated PU film (c) by TSE and (d) through SSAR followed by TSE.

throughout the PU nanocomposites. A more detailed examination of these spherulites in the PU matrix with various hybrid 3D nanofillers unveiled distinct differences in their morphologies. The 2D fillers in TPU gave rise to lamellar-type nanoscale structures, but during the formation of nanocomposites through SSAR, both of these nanoscale building blocks came together to form micron-sized spherulites. Previous studies have indicated that the flat surface of graphene fosters better interaction with the matrix, resulting in a rigid nanocomposite geometry. In contrast, CNTs embedded within the polymer matrix exhibit flexibility and establish point-type contact with the matrix due to their small junction areas.<sup>62</sup> The flexibility of 1D nanofillers within TPU constrains spherulite growth. However, when CNTs are integrated into graphene flakes, they act as bridges, introducing additional rigidity to the TPU. This increased rigidity catalyzes the formation of globular morphology. It's worth noting that the spherulites in TPU, originating from PU nanocomposite films incorporating 2 wt% hybrid 3D nanofillers *via* TSE and through SSAR followed by TSE, exhibit different topological structures. Furthermore, the size of the spherulites was observed to decrease in the PU nanocomposite prepared through SSAR followed by TSE.

#### 4.7. Raman analysis

Fig. 8(a and b) present Raman spectra of both the 3D nanofiller and the prepared nanocomposites. The Raman spectrum of the hybrid 3D nanofiller and the nanocomposites exhibits two distinct features: (i) a G-band at 1582 cm<sup>-1</sup>, corresponding to the  $E_{2g}$  symmetry phonon mode of sp<sup>2</sup> hybridized carbon atoms and (ii) a D-band at 1346 cm<sup>-1</sup>, indicating the presence of defects in the hybrid 3D nanofiller due to functionalized carbon nanotubes (CNTs) and graphene.<sup>56</sup> These defects arise from specific structural alterations, primarily involving a shift from sp<sup>2</sup> to sp<sup>3</sup> hybridization in graphene carbon atoms, which occur during the functionalization process.<sup>61</sup>

The intensity ratio ( $I_d/I_g$ ) between these two bands in the hybrid 3D nanofiller was measured at approximately 1.06. Importantly, these  $I_d/I_g$  ratios remained relatively consistent across various nanocomposites that contained varying proportions of hybrid 3D nanofillers mixed into the TPU matrix. In the Raman spectra of PU, characteristic signals associated with distinct molecular vibrations were observed, including bending of C–O–C at 811 cm<sup>-1</sup>, stretching of C–O–C at 1035 cm<sup>-1</sup>, bending of CH<sub>2</sub> at 1444 cm<sup>-1</sup> and stretching of CH<sub>2</sub> at 2854 and 2922 cm<sup>-1</sup>.<sup>63</sup> These signals were clearly visible in the Raman spectra of the neat PU (TPU). However,



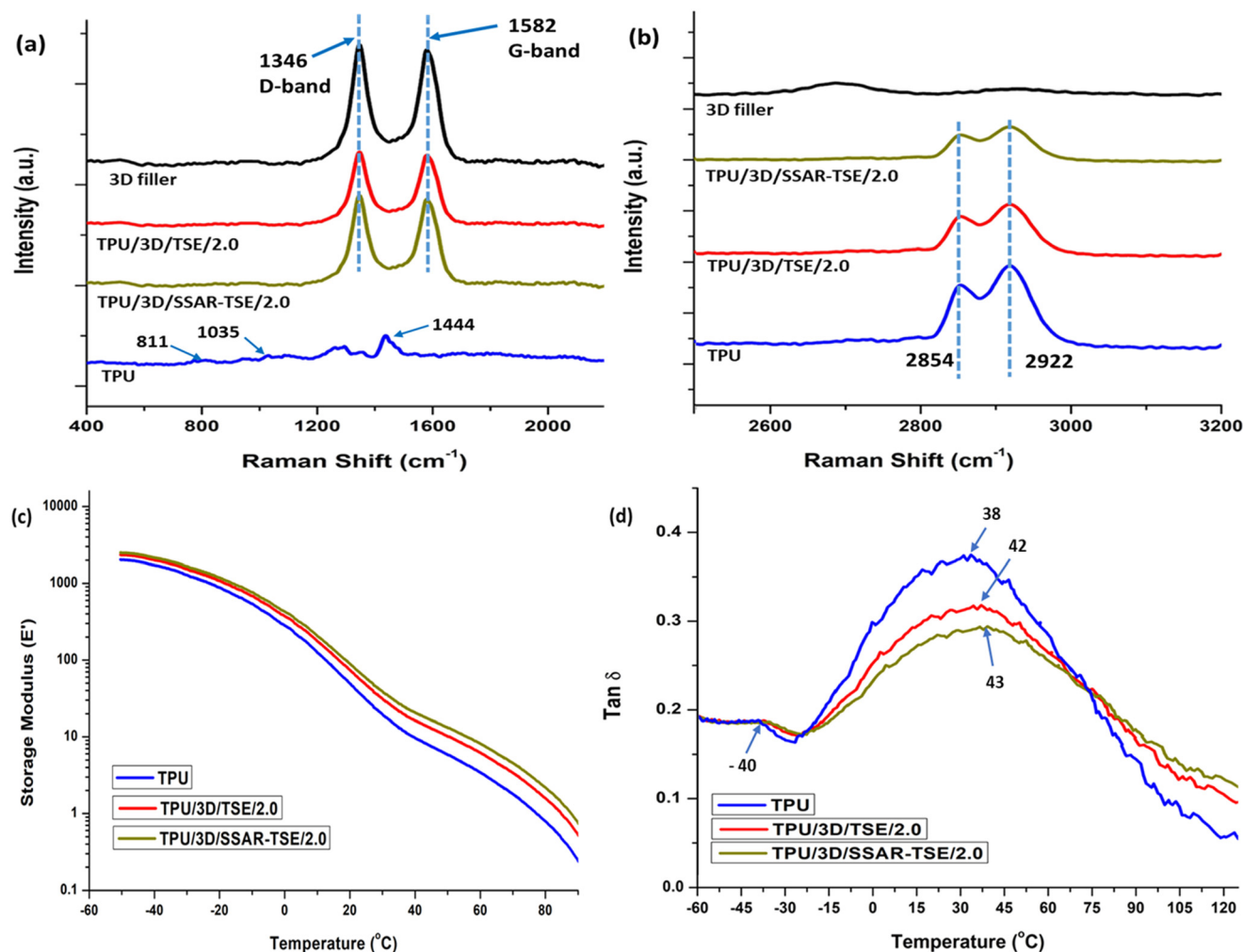


**Fig. 8** Raman spectra of neat thermoplastic polyurethane (TPU, blue color); 2 wt% hybrid 3D nanofiller incorporated TPU by TSE (TPU/3D/TSE/2.0, red color) and through SSAR followed by TSE (TPU/3D/SSAR-TSE/2.0, dark yellow color) in the range 400–2200 cm<sup>-1</sup> (a), and 2400–3200 cm<sup>-1</sup> (b). DMA curves for the storage modulus (c) and tan δ (d) of neat thermoplastic polyurethane (TPU, blue color); 2 wt% hybrid 3D nanofiller incorporated TPU by TSE (TPU/3D/TSE/2.0, red color) and through SSAR followed by TSE (TPU/3D/SSAR-TSE/2.0, dark yellow color).

it was noted that the intensity of the signals corresponding to the stretching of CH<sub>2</sub> at 2854 and 2922 cm<sup>-1</sup> (ref. 63) decreased as the concentration of the hybrid 3D nanofiller increased in the PU matrix. This reduction in signal intensity is attributed to the constrained mobility of the polymer chains in thermoplastic polyurethane (TPU) caused by the increased presence of the hybrid 3D nanofiller in the PU matrix. The higher intensity indicates no or less interaction with the urethane groups of TPU chains and functional groups of 3D fillers. The reduced intensity indicates the concentration of FLGs in the TPU nanocomposites.<sup>47</sup> The constrained mobility of the polymer chains was aroused due to the interactions between functional groups of hybrid 3D fillers and urethane group of TPU indicating the exfoliation of FLGs. The higher exfoliation of FLGs in TPU/3D/SSAR-TSE/2.0 showed highly reduced permeability of the He gas compared to the TPU/3D/TSE/2.0 nanocomposite film.

#### 4.8. DMA analysis

Fig. 8(c and d) provide insights into the storage modulus and glass transition temperature ( $T_g$ ) behavior of different samples, including neat polyurethane (TPU), polyurethane nanocomposites with 2 wt% hybrid 3D nanofiller incorporated by TSE (TPU/3D/TSE/2.0), and hybrid 3D nanofillers prepared through SSAR followed by TSE (TPU/3D/SSAR-TSE/2.0). In the sub-zero temperature range, the storage modulus showed relatively consistent behavior for both neat PU and PU nanocomposites. A distinct feature was observed in the tan δ curve, specifically a peak at around -40 °C for all samples. This peak indicates the  $T_g$  of the soft segments of PU, and its presence was consistent across all samples. The significant variation in  $T_g$  was noted in the hard segment regions of PU, as evident from tan δ peaks at different temperatures – neat PU exhibited a  $T_g$  peak at 38 °C, TPU nanocomposites TPU/3D/TSE/2.0 and TPU/3D/SSAR-TSE/2.0



showed  $T_g$  peaks at 42 °C and 43 °C, respectively. This indicates that the incorporation of hybrid 3D nanofillers primarily influenced the  $T_g$  of the hard segment regions of PU. This effect is likely attributed to hydrogen bonding interactions between the hydroxyl groups of the nanofillers and the urethane linkages of PU's hard segments. Additionally, the  $\tan\delta$  values slightly decreased for all nanocomposites, suggesting increased elasticity or reduced viscous flow compared to neat PU. This improvement is likely a result of effective nanofiller dispersion within the PU matrix, leading to enhanced interactions between the components.<sup>64</sup> In the case of CS4, a modest increase (approximately 5 °C) in the  $T_g$  value of hard segments and a reduction in the  $\tan\delta$  value were observed. These findings suggest reduced polymer chain mobility in the nanocomposites compared to neat PU,<sup>64–66</sup> which could be advantageous for improving the material's gas barrier properties.

## 5. Conclusions

In this research, a combination of SSAR followed by TSE and direct TSE processes was employed to create polyurethane (PU) nanocomposite films reinforced with hybrid 3D nanofillers. The strong hydrogen bonding interactions between PU and the hybrid 3D nanofillers played a pivotal role in achieving a high degree of nanofiller dispersion within the PU matrix, consequently enhancing the gas barrier properties of the PU nanocomposite films. As the concentration of few-layer graphene within the hybrid 3D nanofiller increased, there was a gradual reduction in helium gas permeability values for the PU nanocomposite films. However, the experimental results did not conform to any specific predictive gas permeability model, primarily due to differences in assumptions and the actual state of hybrid 3D nanofiller dispersion within the PU matrix at higher loadings (5 wt%). The 2 wt% hybrid 3D nanofiller-reinforced polyurethane nanocomposite (TPU/3D/SSAR-TSE/2.0) film exhibited excellent gas barrier performance, reducing helium gas permeability by a substantial 63%. At specific concentrations, particularly up to 2.0 wt% of hybrid 3D nanofillers, the nanoplatelets exhibited partial exfoliation and uniform dispersion, leading to a significant reduction in gas permeability that aligned with the predictions of the Cussler-random array model for nanofillers with aspect ratios of 180 and 90. Nevertheless, as the concentration of hybrid 3D nanofillers increased further, the actual gas permeability values deviated from the predictions of any particular model. This discrepancy could be attributed to changes in the dispersion state of hybrid 3D nanofillers within the PU matrix and the tendency for slight agglomeration at higher loadings (5 wt%). The evaluation made through ATR-FTIR, SEM, TEM, XRD, Raman analysis, DMA analysis and AFM techniques collectively confirmed the improved gas barrier properties attributed to the presence of hydrogen bonding

and enhanced interaction between the hybrid 3D nanofiller and the PU matrix.

## Conflicts of interest

There are no conflicts to declare.

## Acknowledgements

The authors are thankful to the Director, DMSRDE, Defence Research and Development Organization for encouragement, support and giving permission to publish the article. The authors are very grateful to Dr. Bapan Adak (former PhD Scholar, IIT Delhi) for helping to prepare the samples by TSE and film preparation by compression molding, Mr. Uttam Saha (for ATR-FTIR), from DMSRDE, Kanpur (DRDO). The authors are also thankful to ADRDE, Agra (DRDO) for providing the facility for helium gas permeability testing. The authors are very thankful to Nano Research Centre (NRC), IIT Kanpur, India (for providing FE-SEM facility).

## References

- 1 M. Joshi, B. Adak and B. S. Butola, Polyurethane nanocomposite-based gas barrier films, membranes, and coatings: a review on synthesis, characterization and potential applications, *Prog. Mater. Sci.*, 2018, **97**, 230–282, DOI: [10.1016/j.pmatsci.2018.05.001](https://doi.org/10.1016/j.pmatsci.2018.05.001).
- 2 S. Y. Huang, C. W. Lou, R. Yan, Q. Lin, T. T. Li and Y. S. Chen, Investigation on structure and impact-resistance property of polyurethane foam filled three-dimensional fabric reinforced sandwich flexible composites, *Composites, Part B*, 2017, **131**, 43–49, DOI: [10.1016/j.compositesb.2017.07.061](https://doi.org/10.1016/j.compositesb.2017.07.061).
- 3 G. Rossignolo, G. Malucelli and A. Lorenzetti, Recycling of polyurethanes: where we are and where we are going, *Green Chem.*, 2024, **26**, 1132–1152, DOI: [10.1039/D3GC02091F](https://doi.org/10.1039/D3GC02091F).
- 4 H. Zhai and A. Euler, Material challenges for lighter-than-air systems in high altitude applications, *AIAA 5th Aviat. Technol. Integr. Oper. Conf.*, Arlington, Virginia, 2005, pp. 1–12.
- 5 V. Mittal, Elastomer Clay Nanocomposites for Packaging, in *Recent Adv. Elastomeric Nanocomposites*, ed. V. Mittal, J. K. Kim and K. Pal, Springer, Berlin, Heidelberg, 2011, vol. 9, pp. 233–256.
- 6 G. Shamini and K. Yusoh, Gas Permeability Properties of Thermoplastic Polyurethane Modified Clay Nanocomposites, *Int. J. Chem. Eng. Appl.*, 2014, **5**, 64–68, DOI: [10.7763/IJCEA.2014.V5.352](https://doi.org/10.7763/IJCEA.2014.V5.352).
- 7 Y. Qian, C. I. Lindsay, C. MacOsco and A. Stein, Synthesis and properties of vermiculite-reinforced PU nanocomposites, *ACS Appl. Mater. Interfaces*, 2011, **3**, 3709–3717, DOI: [10.1021/am2008954](https://doi.org/10.1021/am2008954).
- 8 P. Kaveh, M. Mortezaei, M. Barikani and G. Khanbabaei, Low-Temperature Flexible Polyurethane/Graphene Oxide Nanocomposites: Effect of Polyols and Graphene Oxide on Physicomechanical Properties and Gas Permeability, *Polym.-*





- Plast. Technol. Eng.*, 2014, **53**, 278–289, DOI: [10.1080/03602559.2013.844241](#).
- 9 L. W. McKeen, *Permeability Properties of Plastics and Elastomers*, William Andrew, Oxford, UK, 4th edn, 2016.
  - 10 L. K. Massey, *Permeability properties of plastics and elastomers: a guide to packaging and barrier materials*, William Andrew, 2nd edn, 2003.
  - 11 R. Xu, E. Manias, A. J. Snyder and J. Runt, Low permeability biomedical PU nanocomposites, *J. Biomed. Mater. Res., Part A*, 2003, **64**, 114–119, DOI: [10.1002/jbm.a.10377](#).
  - 12 K. Narayanasamy, S. S. Sekar, R. Rajakumari, R. K. Suresh, D. Roy and K. Dinakaran, Synthesis and characterization of Ag/Au-MnO<sub>2</sub> nanostructure embedded polyvinylidene difluoride high K nanocomposites, *Int. J. Polym. Anal. Charact.*, 2021, **26**, 37–46, DOI: [10.1080/1023666X.2020.1840864](#).
  - 13 K. Bagdi, K. Molnár, I. Sajó and B. Pukánszky, Specific interactions, structure and properties in segmented PU elastomers, *eXPRESS Polym. Lett.*, 2011, **5**, 417–427, DOI: [10.3144/expresspolymlett.2011.41](#).
  - 14 A. P. Isfahani, B. Ghalei, R. Bagheri, Y. Kinoshita, H. Kitagawa and E. Sivanian, Polyurethane gas separation membranes with ethereal bonds in the hard segments, *J. Membr. Sci.*, 2016, **513**, 58–66, DOI: [10.1016/j.memsci.2016.04.030](#).
  - 15 K. Ulubayram and N. Hasirci, Polyurethanes – Effect of Chemical-Composition on Mechanical-Properties and Oxygen Permeability, *Polymer*, 1992, **33**, 2084–2088, DOI: [10.1016/0032-3861\(92\)90874-V](#).
  - 16 Z. F. Wang, B. Wang, N. Qi, X. M. Ding and J. L. Hu, Free volume and water vapor permeability properties in PU membranes studied by positrons, *Mater. Chem. Phys.*, 2004, **88**, 212–216, DOI: [10.1016/j.matchemphys.2004.07.012](#).
  - 17 Y. Wang, M. Gupta and D. A. Schiraldi, Oxygen permeability in thermoplastic Pus, *J. Polym. Sci., Part B: Polym. Phys.*, 2012, **50**, 681–693, DOI: [10.1002/polb.23053](#).
  - 18 P. K. Maji, N. K. Das and A. K. Bhowmick, Preparation and properties of PU nanocomposites of novel architecture as advanced barrier materials, *Polymer*, 2010, **51**, 1100–1110, DOI: [10.1016/j.polymer.2009.12.040](#).
  - 19 H. Kim, Y. Miura and C. W. MacOsco, Graphene/PU nanocomposites for improved gas barrier and electrical conductivity, *Chem. Mater.*, 2010, **22**, 3441–3450, DOI: [10.1021/cm100477v](#).
  - 20 J. K. Pandey, K. R. Reddy, A. K. Mohanty and M. Misra, *Handbook of polymernanocomposites, processing, performance and application volume A: Layered silicates*, Springer, Berlin, Heidelberg, 2013.
  - 21 C. Xiang, P. J. Cox, A. Kukovecz, B. Genorio, D. P. Hashim and Z. Yan, Functionalized low defect graphene nanoribbons and PU composite film for improved gas barrier and mechanical performances, *ACS Nano*, 2013, **7**, 10380–10386, DOI: [10.1021/nn404843n](#).
  - 22 M. Stratigaki, G. Choudalakis and A. D. Gotsis, Gas transport properties in waterborne polymer nanocomposite coatings containing organomodified clays, *J. Coat. Technol. Res.*, 2014, **11**, 899–911, DOI: [10.1007/s11998-014-9594-7](#).
  - 23 K. Madhavan, D. Gnanasekaran and B. S. R. Reddy, Poly(dimethylsiloxane-urethane) membranes: Effect of linear siloxane chain and caged silsesquioxane on gas transport properties, *J. Polym. Res.*, 2011, **18**, 1851–1861, DOI: [10.1007/s10965-011-9592-8](#).
  - 24 S. Cai, F. M. Allieux, J. Tang, J. Han, J. Zhang, Y. He, S. Merhebi, M. J. Christoe, M. Mayyas, E. H. Wong and C. Boyer, Soft liquid metal infused conductive sponges, *Adv. Mater. Technol.*, 2022, **7**(8), 2101500.
  - 25 T. Bansala, M. Joshi, S. Mukhopadhyay, R. A. Doong and M. Chaudhary, Electrically conducting graphene-based polyurethane nanocomposites for microwave shielding applications in the Ku band, *J. Mater. Sci.*, 2017, **52**, 1546–1560, DOI: [10.1007/s10853-016-0449-8](#).
  - 26 P. Chamoli, M. K. Das and K. K. Kar, Green synthesis of silver-graphene nanocomposite based transparent conducting film, *Phys. E*, 2017, **90**, 76–84, DOI: [10.1016/j.physe.2017.03.015](#).
  - 27 F. Guo, G. Silverberg, S. Bowers, S. P. Kim, D. Datta and V. Shenoy, Graphene-based environmental barriers, *Environ. Sci. Technol.*, 2012, **14**, 7717–7724, DOI: [10.1021/es301377y](#).
  - 28 V. Berry, Impermeability of graphene and its applications, *Carbon*, 2013, **62**, 1–10, DOI: [10.1016/j.carbon.2013.05.052](#).
  - 29 H. Liu, J. Wu, C. Liu, B. Pan, N. H. Kim and J. H. Lee, Differently-charged graphene-based multilayer films by a layer-by-layer approach for oxygen gas barrier application, *Composites, Part B*, 2018, **155**, 391–396, DOI: [10.1016/j.compositesb.2018.08.137](#).
  - 30 S. Kumar, H. Arumugham, D. Roy and D. Kannaiyan, Synthesis and characterization of fluorine functionalized graphene oxide dispersed quinoline-based polyimide composites having low-k and UV shielding properties, *Polym. Adv. Technol.*, 2022, **33**, 427–439, DOI: [10.1002/pat.5527](#).
  - 31 L. J. Van Rooyen, J. Karger-Kocsis and L. D. Kock, Improving the helium gas barrier properties of epoxy coatings through the incorporation of graphene nanoplatelets and the influence of preparation techniques, *J. Appl. Polym. Sci.*, 2015, **132**(39), DOI: [10.1002/app.42584](#).
  - 32 J. G. Wijmans and R. W. Baker, The solution-diffusion model: a review, *J. Membr. Sci.*, 1995, **107**, 1–21, DOI: [10.1016/0376-7388\(95\)00102-I](#).
  - 33 L. E. Nielsen, Models for the Permeability of Filled Polymer Systems, *J. Macromol. Sci., Chem.*, 1967, **1**, 929–942, DOI: [10.1080/10601326708053745](#).
  - 34 R. K. Bharadwaj, Modeling the barrier properties of polymer-layered silicate nanocomposites, *Macromolecules*, 2001, **34**, 9189–9192, DOI: [10.1021/ma010780b](#).
  - 35 E. L. Cussler, S. E. Hughes, W. J. Ward and R. Aris, Barrier membranes, *J. Membr. Sci.*, 1988, **38**, 161–174, DOI: [10.1016/S0376-7388\(00\)80877-7](#).
  - 36 G. H. Fredrickson and J. Bicerano, Barrier properties of oriented disk composites, *J. Chem. Phys.*, 1999, **110**, 2181–2188, DOI: [10.1063/1.477829](#).



- 37 B. M. Yoo, H. J. Shin, H. W. Yoon and H. B. Park, Graphene and graphene oxide and their uses in barrier polymers, *J. Appl. Polym. Sci.*, 2014, **131**, 1–23, DOI: [10.1002/app.39628](#).
- 38 A. Hiltner, R. Y. F. Liu, Y. S. Hu and E. Baer, Oxygen transport as a solid-state structure probe for polymeric materials: A review, *J. Polym. Sci., Part B: Polym. Phys.*, 2005, **43**, 1047–1063, DOI: [10.1002/polb.20349](#).
- 39 K. Yano, A. Usuki, A. Okada, T. Kurauchi and O. Kamigaito, Synthesis and properties of polyimide-clay hybrid, *J. Polym. Sci., Part A: Polym. Chem.*, 1993, **31**, 2493–2498, DOI: [10.1002/pola.1993.080311009](#).
- 40 S. Mandal, D. Roy, N. E. Prasad and M. Joshi, Interfacial interactions and properties of cellular structured polyurethane nanocomposite based on carbonaceous nanofillers, *J. Appl. Polym. Sci.*, 2021, **138**, 49775, DOI: [10.1002/app.49775](#).
- 41 A. S. R. Nair, S. Mandal, D. Roy and N. E. Prasad, Fabrication of cellular structures in thermoplastic polyurethane matrix using carbonaceous nanofillers, *IOP Conf. Ser.: Mater. Sci. Eng.*, 2022, **1219**, 012004.
- 42 S. Mandal, D. Roy, K. Mukhopadhyay, M. Dwivedi and M. Joshi, Large-scale dispersion of the hierarchical (1D, 2D and 3D) carbonaceous nanofillers in thermoplastic polyurethane through supramolecular self-assembly and extrusion, *Compos. Interfaces*, 2023, 1–24.
- 43 P. Pokharel, B. Pant, K. Pokhrel, H. R. Pant, J. G. Lim and D. S. Lee, Effects of functional groups on the graphene sheet for improving the thermomechanical properties of polyurethane nanocomposites, *Composites, Part B*, 2015, **78**, 192–201, DOI: [10.1016/j.compositesb.2015.03.089](#).
- 44 H. Kim, A. A. Abdala and C. W. MacOsco, Graphene/polymer nanocomposites, *Macromolecules*, 2010, **43**, 6515–6530, DOI: [10.1021/ma100572e](#).
- 45 J. N. Gavvani, H. Adelnia and M. M. Gudarzi, Intumescent flame-retardant PU/reduced graphene oxide composites with improved mechanical, thermal, and barrier properties, *J. Mater. Sci.*, 2014, **49**, 243–254.
- 46 N. Yousefi, M. M. Gudarzi, Q. Zheng, X. Lin, X. Shen and J. Jia, *et al.*, Highly aligned, ultralarge-size reduced graphene oxide/PU nanocomposites: Mechanical properties and moisture permeability, *Composites, Part A*, 2013, **49**, 42–50, DOI: [10.1016/j.compositesa.2013.02.005](#).
- 47 B. Adak, M. Joshi and B. S. Butola, Polyurethane/functionalized-graphene nanocomposite films with enhanced weather resistance and gas barrier properties, *Composites, Part B*, 2019, **176**, 107303.
- 48 U. Chatterjee, B. S. Butola and M. Joshi, High energy ball milling for the processing of organo-montmorillonite in bulk, *Appl. Clay Sci.*, 2017, **140**, 10–16, DOI: [10.1016/j.clay.2017.01.019](#).
- 49 B. Adak, B. S. Butola and M. Joshi, Effect of organoclay-type and clay-polyurethane interaction chemistry for tuning the morphology, gas barrier and mechanical properties of clay/polyurethane nanocomposites, *Appl. Clay Sci.*, 2018, **161**, 343–353, DOI: [10.1016/j.clay.2018.04.030](#).
- 50 S. Nazarenko, P. Meneghetti, P. Julmon, B. G. Olson and S. Qutubuddin, Gas barrier of polystyrene montmorillonite clay nanocomposites: Effect of mineral layer aggregation, *J. Polym. Sci., Part B: Polym. Phys.*, 2007, **45**, 1733–1753, DOI: [10.1002/polb.21181](#).
- 51 R. K. Layek, M. E. Uddin, N. H. Kim, A. K. T. Lau and J. H. Lee, Noncovalent functionalization of reduced graphene oxide with pluronic F127 and its nanocomposites with gum Arabic, *Composites, Part B*, 2017, **128**, 155–163, DOI: [10.1016/j.compositesb.2017.07.010](#).
- 52 A. V. Menon, G. Madras and S. Bose, Ultrafast self-healable interfaces in polyurethane nanocomposites designed using diels-alder “click” as an efficient microwave absorber, *ACS Omega*, 2018, **3**, 1137–1146, DOI: [10.1021/acsomega.7b01845](#).
- 53 M. Ioniță, G. M. Vlăsceanu, A. A. Watzlawek, S. I. Voicu, J. S. Burns and H. Iovu, Graphene and functionalized graphene: Extraordinary prospects for nanobiocomposite materials, *Composites, Part B*, 2017, **121**, 34–57, DOI: [10.1016/j.compositesb.2017.03.031](#).
- 54 B. Adak, M. Joshi and B. S. Butola, Polyurethane/clay nanocomposites with improved helium gas barrier and mechanical properties: direct versus master-batch melt mixing route, *J. Appl. Polym. Sci.*, 2018, **135**, 46422, DOI: [10.1002/app.46422](#).
- 55 X. F. Yang, C. Vang, D. E. Tallman, G. P. Bierwagen, S. G. Croll and S. Rohlik, Weathering degradation of a polyurethane coating, *Polym. Degrad. Stab.*, 2001, **74**, 341–351, DOI: [10.1016/S0141-3910\(01\)00166-5](#).
- 56 F. T. Johra, J. W. Lee and W. G. Jung, Facile and safe graphene preparation on solution based platform, *J. Ind. Eng. Chem.*, 2014, **20**, 2883–2887, DOI: [10.1016/j.jiec.2013.11.022](#).
- 57 H. C. Kuan, C. C. Ma, W. P. Chang, S. M. Yuen, H. H. Wu and T. M. Lee, *Compos. Sci. Technol.*, 2005, **65**, 1703–1710, DOI: [10.1016/j.compscitech.2005.02.017](#).
- 58 S. L. Phua, L. Yang, C. L. Toh, S. Huang, Z. Tsakadze, S. K. Lau, Y. W. Mai and X. Lu, *ACS Appl. Mater. Interfaces*, 2012, **4**, 4571–4578, DOI: [10.1021/am300947b](#).
- 59 A. V. Raghu, Y. R. Lee, H. M. Jeong and C. M. Shin, Preparation and physical properties of waterborne polyurethane/functionalized graphene sheet nanocomposites, *Macromol. Chem. Phys.*, 2008, **209**, 2487–2493, DOI: [10.1002/macp.200800395](#).
- 60 L. Chen, H. Yu, J. Zhong, L. Song, J. Wu and W. Su, Graphene field emitters: a review of fabrication, characterization and properties, *Mater. Sci. Eng. B: Solid-State Mater. Adv. Technol.*, 2017, **220**, 44–58, DOI: [10.1016/j.mseb.2017.03.007](#).
- 61 K. N. Kudin, B. Ozbaz, H. C. Schniepp, R. K. Prud'homme, I. A. Aksay and R. Car, Raman spectra of graphite oxide and functionalized graphene sheets, *Nano Lett.*, 2008, **8**, 36–41, DOI: [10.1021/nl071822y](#).
- 62 M. Bera and P. K. Maji, Effect of structural disparity of graphene-based materials on thermo-mechanical and surface properties of thermoplastic polyurethane nanocomposites, *Polymer*, 2017, **119**, 118–133, DOI: [10.1016/j.polymer.2017.05.019](#).



- 63 H. Janik, B. Palys and Z. S. Petrovic, Multiphase-separated polyurethanes studied by micro-Raman spectroscopy, *Macromol. Rapid Commun.*, 2003, **24**, 265–268, DOI: [10.1002/marc.200390039](https://doi.org/10.1002/marc.200390039).
- 64 D. A. Nguyen, A. V. Raghu, J. T. Choi and H. M. Jeong, Properties of thermoplastic polyurethane/functionalised graphene sheet nanocomposites prepared by the in situ polymerisation method, *Polym. Polym. Compos.*, 2010, **18**, 351–358, DOI: [10.1177/096739111001800701](https://doi.org/10.1177/096739111001800701).
- 65 R. Shamsi, M. Koosha and M. Mahyari, Improving the mechanical, thermal and electrical properties of polyurethane-graphene oxide nanocomposites synthesized by in-situ polymerization of ester-based polyol with hexamethylene diisocyanate, *J. Polym. Res.*, 2016, **23**, 1, DOI: [10.1007/s10965-016-1155-6](https://doi.org/10.1007/s10965-016-1155-6).
- 66 D. Roy, N. Tiwari, K. Mukhopadhyay and A. K. Saxena, The effect of a doubly modified carbon nanotube derivative on the microstructure of epoxy resin, *Polymer*, 2014, **55**, 583–593, DOI: [10.1016/j.polymer.2013.12.012](https://doi.org/10.1016/j.polymer.2013.12.012).

